A Computational Study on Diffuser Length Variation for a Ducted Rotor in Hover and Edgewise Flight

Matthew Misiorowski
PhD Candidate
Rensselaer Polytechnic Institute
Troy, New York, USA

Farhan Gandhi
Professor
Rensselaer Polytechnic Institute
Troy, New York, USA

Assad A. Oberai
Professor
Rensselaer Polytechnic Institute
Troy, New York, USA

ABSTRACT

This study examines the effect of diffuser length variation on the performance of ducted rotors in hover and edgewise flight. The flow over a three-dimensional model of ducted rotor configurations was simulated using the Spalart-Allmaras RANS model implemented in a stabilized finite element method. A sliding mesh was used to conveniently account for the large-scale motion associated with rotor revolutions. The simulation results were analyzed to understand the flow physics and quantify the contributions of the rotor and various sections of the duct interior surfaces on the total thrust, drag, and pitching moments. Performance comparisons were made between the different diffuser length configurations, varying from 144% to 18% rotor radius. In hover, the short diffuser configurations produced 3% lower thrust and required 1.5% higher power than the long diffuser configurations. In 10 m/s edgewise flight, the duct inlet at the front generates high lift, and the rotor generates higher lift over the front as well due to the upwash at the front of the disk. These factors combine to generate a large nose-up pitching moment. Additionally, ducted rotors typically see large drag from ram pressure on the rear diffuser. At 10m/s edgewise flight, the rotor was the dominant generator of thrust (in the range of 80% of the total), Reducing diffuser length did not affect the thrust generated by the rotor, but the duct thrust reduced by about a third. The short duct completely eliminated the ram-pressure induced H-force on the rear diffuser, significantly reducing the drag of the entire system. Since the ram pressure on the aft diffuser generated a nose-down moment partially counteracting the nose-up moments from the rotor and duct inlet, its absence in the shortest duct resulted in a net increase in steady nose-up pitching moment. The rotor is the primary source of vertical vibratory forces as well as vibratory pitching moment. The small tip clearance of the rotor causes a local interaction between the blade tip and duct that is the dominant contributor to vibratory H-force on the ducted rotor. The shortest diffuser configuration was shown to significantly reduce the magnitude of the vertical and H-force vibrations, but the magnitude of the vibratory pitching moments increased.

NOMENCLATURE

d	Length of diffuser section
L	Length of exterior duct section
R	Rotor radius
r	Radius of duct inlet curvature
S_x	Blade root shear in the chordwise direction
S_z	Blade root shear in the vertical direction
$y+$	Non-dimensional distance to describe element height
α	Effective angle of attack of the duct cross-section
δ	Rotor blade tip clearance to duct wall
γ	Angle made by diffuser from vertical (Z) direction
θ	Nose down attitude of ducted rotor

INTRODUCTION

Ducted rotor designs like the Boeing Phantom Swift, the Urban Aeronautics X-Hawk, and the Aurora Flight Sciences Lightning Strike employ ducted fans to provide vertical take-off and landing (VTOL) capability and in some cases act as ducted propellers (Refs. 1–3). Ducted fans provide an element of safety over open rotors which makes them desirable for manned vehicles and missions operating near people or buildings. In addition to safety, the duct can provide certain performance improvements compared to an open rotor.

Ducts have been shown to decrease rotor power by expanding the rotor wake through a diffuser section, which reduces the induced power (Ref. 4). Although the expansion of the rotor wake reduces the thrust produced by the rotor as well, air is drawn by the rotor over the duct inlet, causing a suction similar to the lift generated on the leading edge of an airfoil and provides additional thrust. In a well-designed duct, this additional lift will overcompensate for the reduction in rotor thrust, resulting in a ducted rotor that operates at a higher power loading than the same rotor in isolation.

While ducted rotors have proven aerodynamic advantages in hover, they experience large drag and pitching moments in forward flight. When the edgewise flight velocity dominates the inflow velocity, the front of the duct has a large angle of at-

Presented at the AHS International Technical Meeting: Aeromechanics Design for Transformative Vertical Flight, San Francisco, California, USA, Jan 16–19, 2018.

tack and behaves like an airfoil in deep stall, producing large amounts of lift but with flow separation close to the leading edge of the inlet (Ref. 5). Prior experimental and computational research has been conducted analyzing the performance of ducted fans in axial and edgewise flight as well as specific duct designs attempting to mitigate the deep stall behavior of the upstream section of the duct.

Early experiments conducted by Platt (Ref. 6) and Taylor (Ref. 7) measured static rotor thrust while varying the length of the diffuser. In both experiments the ratio of the diffuser exit area to the rotor area is held constant and shows varying the length of the diffuser had little effect on the static thrust. However, both experiments note that this trend may not hold for extremely short diffusers, and a minimum diffuser length is required for the pressure rise across the rotor disk to develop as axial dynamic pressure. This length will be dependent on the specific ducted rotor design.

Pereira and Chopra (Refs. 8, 9) parameterized the duct geometry by inlet curvature, diffuser length and diffuser angle and measured the forces and moments acting on the ducted rotor in axial and edgewise flight. This experiment established trends in ducted rotor performance based on these geometric parameters. The results showed how increasing the radius of curvature of the inlet could delay the separation point on the upstream duct inlet.

Hook, Myers and McLaughlin (Refs. 10, 11) performed experiments on a tandem ducted fan design with two ducted fans arranged longitudinally in the body of an air vehicle. Forces and moments acting on the aircraft were measured and the inlet shape on the front duct was changed attempting to improve vehicle performance. Using flow visualization techniques, this experiment confirmed that altering the inlet design could reduce the separation region on the upstream duct inlet but it did not significantly affect the aircraft lift or drag.

Martin and Tung performed wind tunnel experiments on an isolated ducted fan in axial and edgewise flight. This experiment recorded the forces and moments acting on the ducted fan while the duct inlet curvature was varied (Ref. 12). The experiment also examined the effect of rotor tip clearance with the duct wall. When the rotor RPM was varied in this study, the angle of attack at which stall occurs on the upstream duct inlet changed significantly, demonstrating that a high induced velocity is required to help keep flow attached to the duct inlet in edgewise flight. Martin and Boxwell further investigated the effect tip clearance has on ducted rotor performance by testing notches in the interior of the duct in the rotor plane. (Ref. 13). Ultimately, the notched duct designs did not significantly change the ducted rotor performance.

Akturk and Camci (Refs. 14–16) used a combination of experimental and computational methods to analyze ducted fans. Particle image velocimetry (PIV) and wind tunnel experiments were conducted on ducted fans in hover and edgewise flight. These experiments showed that the inflow at the front of the rotor disk was affected by the size of the separation bubble on the upstream duct inlet. Further computational analysis was conducted by this group to analyze the effect of rotor tip shapes and a double ducted fan design using computational fluid dynamics (CFD). It was found that decreasing tip clearance improved the performance of the ducted fan and the double duct design acts as a duct inlet separation control device.

The US Army Research Laboratory has conducted computational analysis of ducted fans. Singh and Dinavahi (Ref. 17) coupled CFD analysis with an optimization scheme to design the ideal duct shape. Jimenez and Singh (Ref. 18) used CFD analysis to compare the performance of two different rotor and duct geometry pairs. The first study developed a polynomial surrogate model that was able to predict rotor system performance within 3% of the CFD solution. The second study shows that an untwisted rotor performed more efficiently as a ducted rotor than a rotor with ideal twist. This effect comes from the added downwash on the rotor due to the presence of the duct. Both of these computational studies only looked at axial flow of a ducted rotor in hover.

Misiorowski, Gandhi, and Oberai (Refs. 19, 20) used computational analysis to examine isolated and embedded ducted rotors in hover and edgewise flight. These CFD simulations identified dominant flow physics that drove the integrated forces and moments. Additionally, the results examined interactions between the rotor and duct aerodynamics and their contribution to vibratory forces at the blade passage frequency.

In Refs. 19 and 20, the ram pressure on the aft section of the diffuser was identified as a major contributor to the ducted rotor drag in forward flight. The present study seeks to investigate whether the ducted rotor's drag can be reduced by shortening the diffuser, while simultaneously considering its effect on thrust, power, and pitching moments. The study also examines the effect of change in diffuser length on hover performance and vibratory loads in forward flight. The study is conducted using CFD tools to solve the unsteady Reynolds Averaged Navier-Stokes (URANS) equations to provide a quantitative comparison of the performance of the four analyzed diffuser lengths and visualize complex flow features at various regions in the ducted rotor system.

METHOD

Coordinate System

This study uses a South, East, Up right-handed coordinate system. The $+X$ is the direction of aircraft drag (or H-force), $+Y$ is out the right wing or $\Psi = 90^\circ$ and $+Z$ is in the upward vertical direction.

Ducted Rotor Models

The duct geometry was based on the experiments of Pereira and Chopra which parameterizes the duct geometry by the inlet radius of curvature, length of the diffuser section, and angle of the diffuser section (Ref. 8, 9). Figure 1 provides a to-scale drawing of the ducted rotor configuration describing the duct

design parameters, which are given as percentages of the rotor radius (R). The duct is embedded in a larger body as indicated by Figure 1.

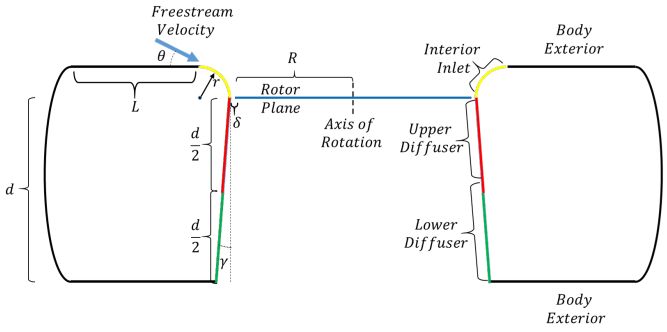

Fig. 1. Schematic of embedded ducted rotor system with parameters describing duct geometry

The parameter r represents the radius of the semicircular inlet section, d represents the length of the entire diffuser section and several diffuser lengths were the focus of this study. The angle γ is the expansion angle of the diffuser section. The parameter δ is exaggerated in the figure for clarity and represents the clearance between the rotor tip and duct wall, and R is the rotor radius. The angle θ is the relative nose down attitude of the ducted rotor relative to the freestream. The values of the duct parameters can be seen in Table 1.

Table 1. Embedded Ducted Rotor Geometry

Duct Parameter	Value
r	26% R
d	144, 72, 36, 18% R
γ	0°
δ	1% R
R	15.24 cm
θ	0°
L	4R

The duct interior was discretized along the axial direction into three surfaces shown in Figure 1: the interior inlet (yellow), the upper diffuser (red) and the lower diffuser (green). For the 72% R, 36% R, and 18% R cases, the diffuser is not separated into upper and lower segments. In addition to discretizing the duct in the axial direction, each of the surfaces is divided azimuthally in 5° increments which provides resolution for determining where around the duct the greatest forces act. A deep ducted fan with a lengthy diffuser section is viable in designs where the fan is embedded in the body of an aircraft such as the Phantom Swift (Ref. 1) or Urban Aeronautics X-Hawk (Ref. 2). However, if the diffuser length were reduced significantly the resulting configuration resembles a shrouded rotor or fan-in-wing such as Project Zero (Ref. 21). The diffuser length is the focus of this study, specifically to determine the effect of its reduction on system performance.

The length L in Figure 1 is not shown to scale and is 4R in the computational model. This length ensures that in forward flight the flow entering the interior inlet is aligned parallel to the rotor plane. To remove the effect of the external aerodynamic faring, all exterior duct sections (black) are not considered. Therefore, only integrated force and moment values for the inlet and diffuser are included in this study.

The rotor used in this study is an APC 12x5.5 MR, a commercially available fixed-pitch propeller for use on small unmanned aerial vehicles (Ref. 22). The rotor is hingeless and assumed to be rigid. The actual rotor blade has a rounded tip, however for the purpose of the study a square tip was used.

This rotor is two bladed and the chord and twist along the span of the blade were measured and tabulated in Table 2. The airfoil sections were assumed to be a NACA 4412 at the root, an Eppler 63 at 20% span, and a Clark Y at the tip, using linear interpolation in between.

Table 2. APC 12x5.5 Blade Geometry

Radial Position (r/R)	Local Chord (cm)	Geometric Twist (degrees)	Airfoil Sections
0	Hub	Hub	NACA 4412
0.1	1.605	20.8	Linear Interp.
0.2	2.393	32.5	Eppler 63
0.3	3.073	27.9	↑
0.4	3.195	21.5	
0.5	3.015	18.0	Linear
0.6	2.751	14.5	Interp.
0.7	2.413	11.0	
0.8	1.958	9.5	↓
0.9	1.455	8.0	
1.0	1.130	6.5	Clark Y

A blade tip to duct wall clearance of 0.1524 cm or 1% R was used in the model. The rotor is assumed to have zero sweep along the line connecting the 50% chord point of each airfoil section. The circular rotor hub is included in the CFD simulation and has a radius of 0.826 cm, resulting in a 5.4% root cutout.

The ducted rotor was simulated in hover and in translational flight conditions of 10 m/s. The rotor speed was maintained at 4300 RPM regardless of flight condition and the ducted fan was oriented at 0° (nose level) pitch attitude. This ducted fan was not trimmed to any flight condition but the resulting lift, drag, pitching moment, etc. are calculated and reported for the prescribed rotor RPM and pitch attitude.

Computational Method

A three-dimensional transient solution to the RANS equations was determined using AcuSolve, a stabilized 2nd order (temporally and spatially) upwind finite element solver specifically designed for incompressible or weakly compressible flows up

to local Mach numbers of 0.8 (Ref. 23). The advancing rotor blade in this study saw freestream Mach numbers less than 0.23 when the ducted rotor translated at 10 m/s, therefore an incompressible solver was suitable. For modeling turbulence a Detached Eddy Simulation (DES) model was used as large separation regions are expected on the inlet in forward flight. DES models have been shown to better capture the separation point of highly separated flows as compared to URANS models (Ref. 24). The Reynolds number for the duct, based on a typical axial speed of 10 m/s (average velocity induced by the rotor) and the height $= d + r = 0.26$ m, was approximately 1.66×10^5. The Reynolds number for the blades based on the chord and the tangential speed at $0.75R$ for 4,300 RPM was approximately 9.19×10^4. The flow at these Reynolds numbers is expected to be transitional for moderate angles of attack. However, given the effective angles of attack are rather large so that significant separation is anticipated and the incoming flow is likely to be unsteady, a turbulent approximation is a reasonable choice.

The computational domain is shown in Figure 2, and an inflow with prescribed velocity and an outflow with zero pressure offset boundary were defined. Other boundaries of the control volume were set to far field which allowed flow to cross the boundary in either direction with no pressure offset. In the hover case, the inflow and outflow were also set to far field.

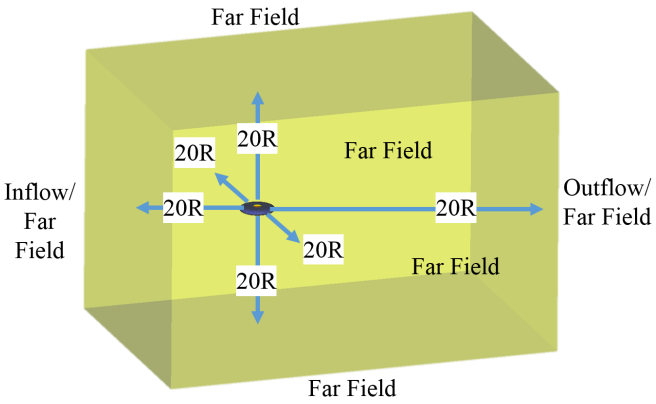

Fig. 2. Computational domain and boundary conditions for embedded duct model

A sliding mesh interface was employed to simulate full rotor revolutions in this study. The sliding mesh method defines two separate volumes inside the computational domain: one volume that rotates with respect to the inertial frame and one that remains stationary. These two volumes are coincident only along the sliding interface surface which passes information between the two volumes. Figure 3 shows the rotating volume (purple) and sliding interface along with the non-rotating volume. The rotating volume is a cylinder centered about the rotor hub; it has a radius of 15.32 cm and extends both above and below the rotor plane by 2.54 cm. The radius of this rotating volume is such that it ends in the middle of the tip gap clearance. The rotor radius is 15.24 cm, this results in 0.0762 cm inside the rotating volume between the rotor tip and the sliding interface and 0.0762 cm between the sliding interface and duct wall in the non-rotating volume.

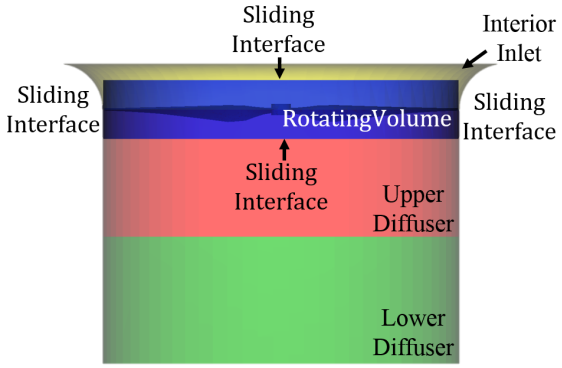

Fig. 3. Sliding interface between the non-rotating volume containing the duct and the rotating volume containing the rotor

The domain was discretized using a meshing software developed by Simmetrix (Ref. 25). The mesh was entirely comprised of unstructured tetrahedral elements. Surface mesh element size control was implemented on the surface of the blades ensuring a maximum element size 1/50th the blade chord. The elements on blade were refined by a factor of $10\times$ in the leading (0-10% chord) and trailing edge (90-100% chord) of the blades, (compared to the elements along the remainder of the chord).

The surface of the duct was also discretized using an unstructured mesh. The size of the surface elements was set to 1/50th the length of the diffuser, this results in an element size corresponding to 2° of rotation. Given the curvature of the interior inlet section the element size was reduced by $10\times$ for this section of the duct. A second refinement region was established on the duct surface near the rotor plane ($\pm 0.1R$), the element size is locally reduced to 0.0254 cm; this is the same size as the elements on the rotor tip as shown in Figure 4.

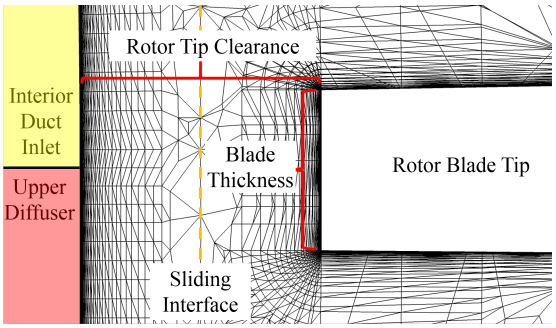

Fig. 4. Cut plane of ducted rotor mesh in the region between the rotor tip and duct wall from looking down the chord of the blade

On both the rotor and the duct a structured boundary layer mesh was employed. The first element height was set to en-

sure $y+ \leq 1$ throughout, estimated using a flat plate at 78 m/s (the advancing blade tip speed). The mesh consisted of 41 million grid points in total with 28 million coming from the rotating volume and 13 million coming from the non-rotating volume.

A mesh refinement study was conducted by varying the following parameters: size of elements along the chord of the rotor, the leading/trailing edge reduction ratio, the aspect ratio of elements along the span of the rotor, the elements along the length of the duct, the local element size near the rotor plane, the azimuthal element size on the duct, and the number of elements in the boundary layer. Each parameter was independently doubled in refinement, convergence was determined when the thrust changed by less than 1% from the previous setting. The values specified in this section are the results of this convergence study.

All cases were run initially using large 10° time steps to let flow develop more quickly, then each simulation was restarted for additional revolutions at 1° time steps until convergence was achieved. The initial 10° time steps are possible without causing solution divergence due to the Streamline Upwind Petrov-Galerkin (SUPG) stabilized finite element method and Generalized α implicit time integration method which is known for suppressing high frequency disturbances and allowing solution stability with Courant−Friedrichs−Lewy (CFL) number > 1 (Refs. 26, 27).

Most runs were performed on 512 2.6 GHz Intel Xeon E5-2650 processors, part of the Center for Computational Innovations (CCI) at Rensselaer Polytechnic Institute. Meshing was completed using the higher memory 3.3 GHz Intel Xeon E5-2643 processor with 256 GB of system memory, also part of the CCI facility.

DIFFUSER LENGTH COMPARISON

A prior study has closely examined the flow physics and performance of an embedded ducted rotor with a deep (144% R) diffuser in hover and forward flight (Ref. 20). The following sections provide a comparison to the results in that study as the diffuser length is varied. The inlet and rotor geometry, rotor speed, flight speed, and nose-level pitch attitude are the same between both configurations. The trade-offs in performance are examined in the following sections.

Hover Performance

The configurations of varying diffuser length were analyzed in hover and compared to the same rotor with the diffuser and inlet completely removed. Consistent with the findings from Refs. 6 and 7, Figure 5 shows that the static thrust produced by the rotor and duct inlet is relatively insensitive to decreasing diffuser length. Decreasing the length of the diffuser to 18% R only decreased the ducted rotor thrust by 3.3% compared to the 144% R diffuser. The open rotor produces more thrust than the ducted rotor, however, the total ducted rotor thrust (sum of duct and rotor thrust) exceeds the open rotor thrust by $\sim$ 26% for the shorter diffusers (18% and 36% R) and by $\sim$ 30% for the longer diffusers (72% and 144% R) as seen in Table 3.

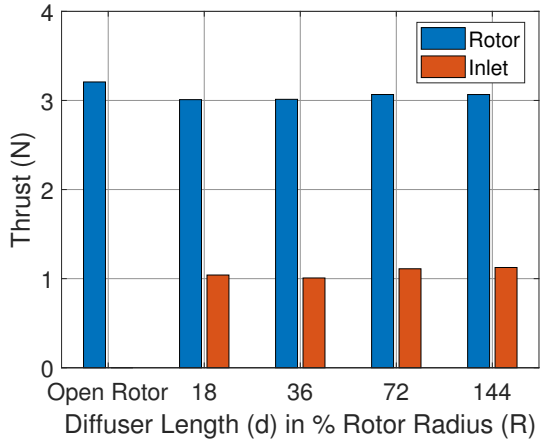

Fig. 5. Thrust produced by the rotor and inlet as diffuser length is varied

Table 3. The total thrust produced and power consumed by each configuration in hover

Configuration	Total Thrust (N)	Power (W)
Open Rotor	3.21	43.00
18% R	4.05	51.68
36% R	4.02	51.79
72% R	4.18	51.03
144% R	4.19	50.94

The rotor power of the 18% R diffuser is $\sim$ 1.5% higher than the 144% R configuration. Additionally, Table 3 shows that the open rotor requires the least power, however, the power loading (thrust divided by power shown in Figure 6) shows that all ducted configurations achieve a higher power loading. The improvement in hover performance is modest with shorter diffusers (18% and 36% R) achieving $\sim$ 5% increase in power loading and longer diffusers (72% and 144% R) achieving $\sim$ 10% increase in power loading over the open rotor.

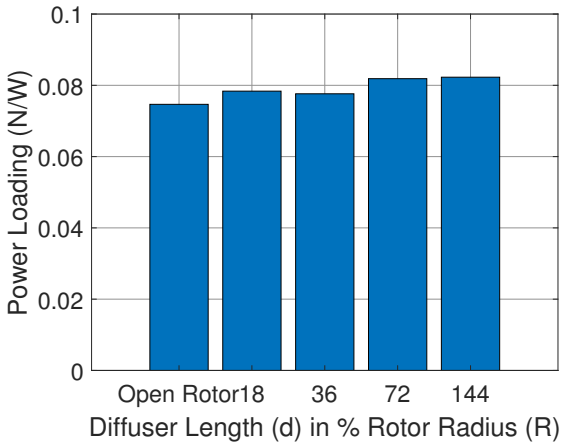

Fig. 6. Power loading of the open and ducted rotor as diffuser length is varied

Forward Flight Performance

For the different duct diffuser lengths, an edgewise flight condition of 10 m/s was considered. As the ducted rotor in this study has zero nose down attitude, the duct interior behaves like the upper/lower surface of an airfoil where the angle of attack is determined by the relative freestream velocity and induced velocity of the rotor, as shown in Figure 7.

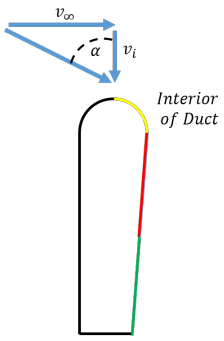

Fig. 7. Effective angle of attack on duct inlet due to freestream velocity and induced inflow

Since the freestream velocity (v_∞) is much larger than the induced velocity (v_i) at the inlet even at moderate flight speeds, the effective angle of attack (α) of the duct inlet is very high which places the forward section of the duct inlet in deep stall. At 10 m/s forward flight speed, flow separates off the duct inlet resulting in an area of low pressure and vorticity in the region of separation (seen in Figure 8 and Figure 9) regardless of diffuser length. The length of the diffuser section does however determine the size of the separation region and behavior of the rotor wake. For the 144% R diffuser shown in Figure 8, the area inside the diffuser where flow is separated off the upstream duct is much larger than for the 18% R case. With regards to the rotor wake, the shorter diffuser allows the rotor wake to convect downstream with less of the wake impinging on the rear diffuser as seen in Figure 9. For ducted rotor configurations with longer diffusers the wake collides with the rear diffuser and is redirected downward in the axial direction (Figure 8). The size of the separation region at the front and the wake impingement at the rear of the duct significantly affect the performance for different diffuser lengths.

Rotor Aerodynamics

Figure 10 shows that in edgewise flight the peak rotor thrust is generated at the front of the disk for all diffuser lengths. The flow separation region results in an area of recirculation near the rotor plane (Figure 8 and Figure 9). This induces an upwash through the rotor plane over the front portion of the disk. The cut plane in Figure 8 and Figure 9 is along the $\Psi = 0^\circ - 180^\circ$ line while the blades are at 90° and 270°. When the blade rotates through the front of the disk, it will see an upwash on the outboard sections. The upwash increases the effective angle of attack locally to produces more lift in this region. This is confirmed by the distribution shown in the disk plots of rotor thrust (Figure 10). Note that the location of the maximum thrust is closer to the front of the disk for the 144% R duct but the peak thrust moves closer to $\Psi = 135^\circ$ as the diffuser length decreases. A secondary effect on the thrust distribution is a decrease in thrust from the rear of the disk as the diffuser length reduces.

The disk plots of blade elemental drag in Figure 11 show the difference of the duct configurations at 10 m/s forward flight speed. These plots show that the drag on the rotor is highest near the midspan on the advancing side, the location with the highest geometric pitch, chord, and dynamic pressure. The peak drag on the advancing blade is seen to increase as the diffuser becomes shorter. Although the front of the disk sees the highest lift, the upwash in that region reduces the induced drag on the blade, which in turn limits the total blade drag. The drag also reduces on the retreating side of the disk (towards the rear) as the diffuser length reduces. This is a result of lower rotor thrust produced in this region of the disk and a reduction in induced drag.

Duct Aerodynamics

Mean forces and moments were calculated by averaging loads over the final revolution. The dominant forces acting on the duct are the thrust and drag (H-force), and the dominant moment is nose-up pitch. All moments presented in this study are taken about the rotor hub. The pitching moment arises from longitudinal asymmetry of the thrust and H-force around the duct on the inlet and diffuser sections.

Figure 12 shows the azimuthal distribution of the duct thrust at 10 m/s forward speed for the 144% R, 72% R, 36% R, and 18% R diffuser lengths. In forward flight, thrust on the duct is produced primarily on the front inlet with no significant contribution from the diffuser section. Even with the front half of the duct behaving like the leading edge of an airfoil in deep stall and the flow separating off the inlet, the duct inlet produces a significant amount of lift. The thrust produced by the front inlet was reduced by decreasing the diffuser length as seen in Figure 12.

Figure 13 shows the azimuthal distribution of H-force on the duct. In forward flight duct drag comes primarily from two sources, the suction on the front inlet and the ram pressure from the stagnation of the freestream on the rear of the duct (primarily on the upper diffuser). At the front of the duct, the radial component of suction on the inlet acts in the direction of aircraft drag. The front diffuser section(s) of the longer diffuser configurations (144% R and 72% R), provide a small propulsive force partially canceling the drag on the front inlet. The propulsive force acting on the front of the diffuser comes from the average value of high pressure on the lower surface of the blades interacting with the diffuser at 2/rev. The interaction between the blade and duct will be further explained in the vibratory loads section.

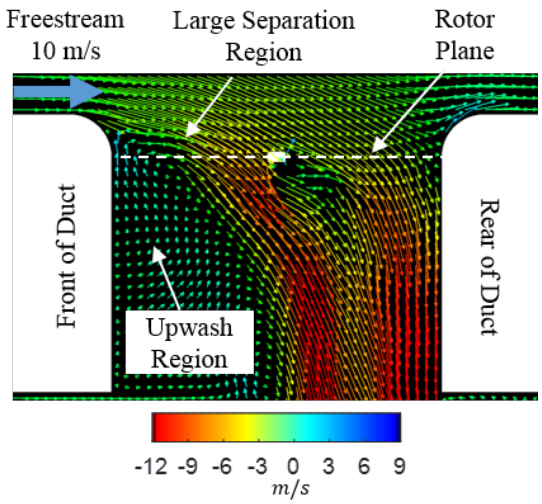

Fig. 8. Velocity vectors of flow through $d = 144\%R$

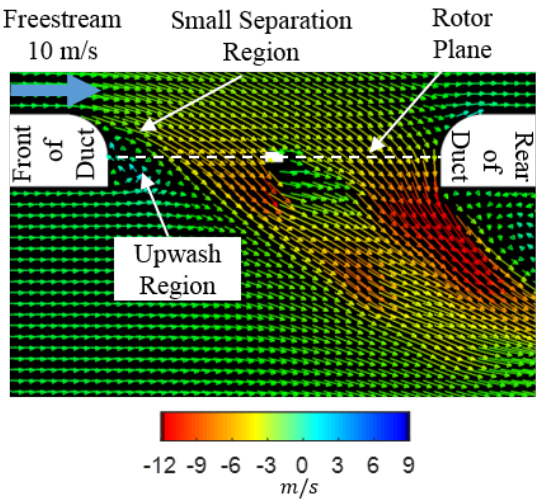

Fig. 9. Velocity vectors of flow through $d = 18\%R$

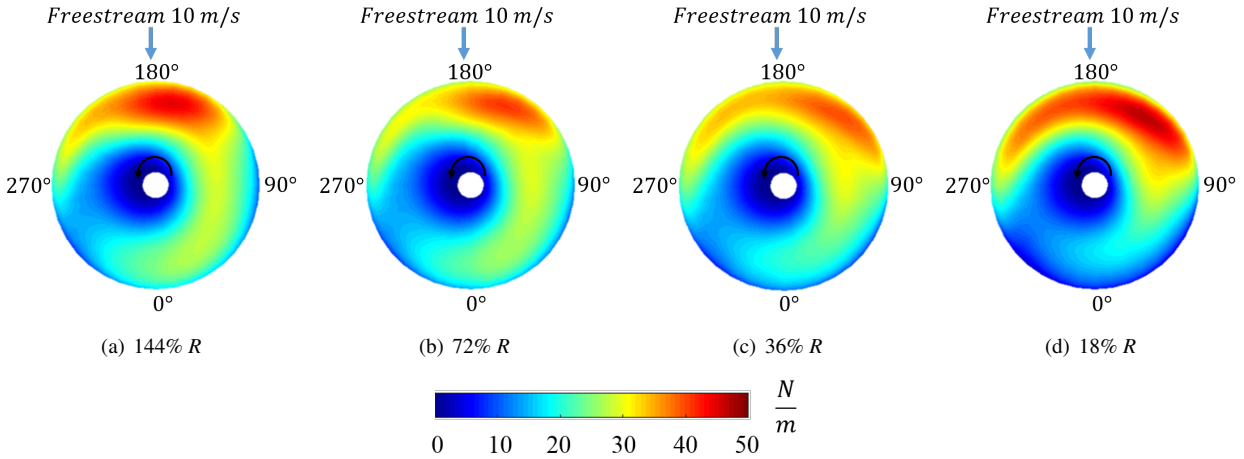

(a) 144% R (b) 72% R (c) 36% R (d) 18% R

Fig. 10. Blade elemental thrust of the ducted rotor at 10 m/s forward flight conditions with various diffuser lengths

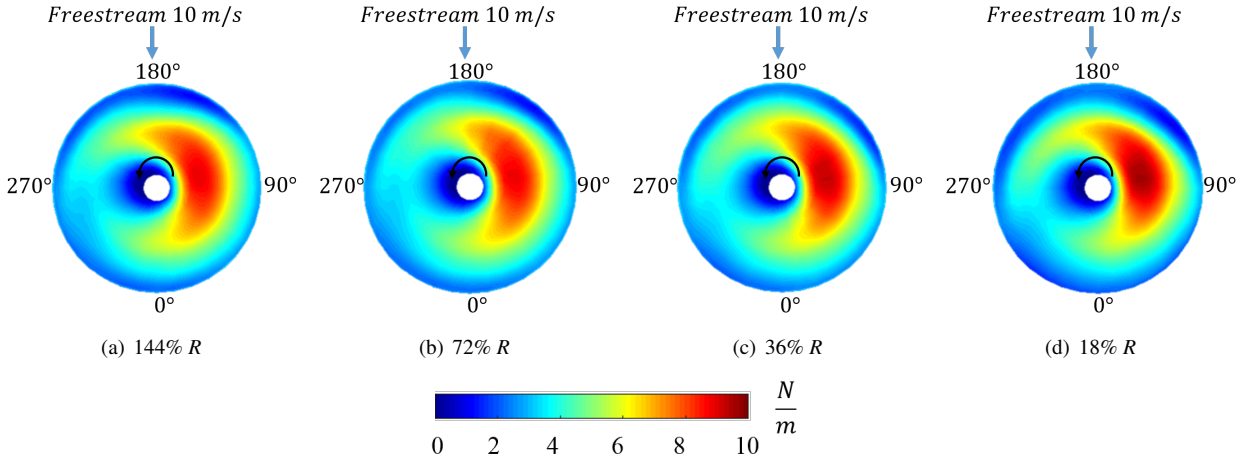

(a) 144% R (b) 72% R (c) 36% R (d) 18% R

Fig. 11. Blade elemental drag of the ducted rotor at 10 m/s forward flight conditions with various diffuser lengths

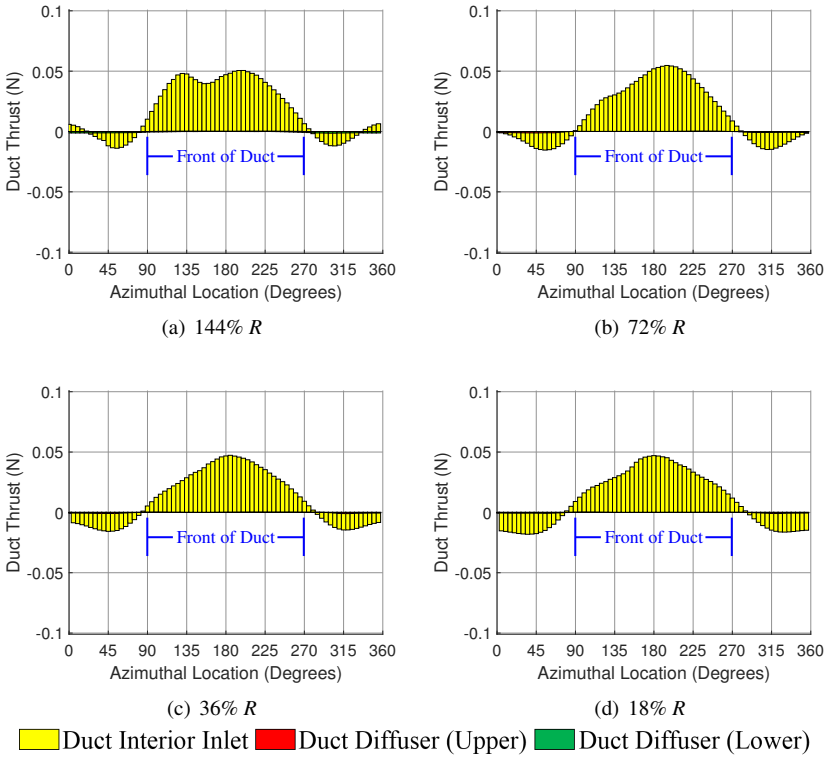

(a) 144% R (b) 72% R

(c) 36% R (d) 18% R

Duct Interior Inlet Duct Diffuser (Upper) Duct Diffuser (Lower)

Fig. 12. Azimuthal breakup of duct thrust at 10 m/s forward flight conditions averaged over one rotor revolution for various diffuser lengths

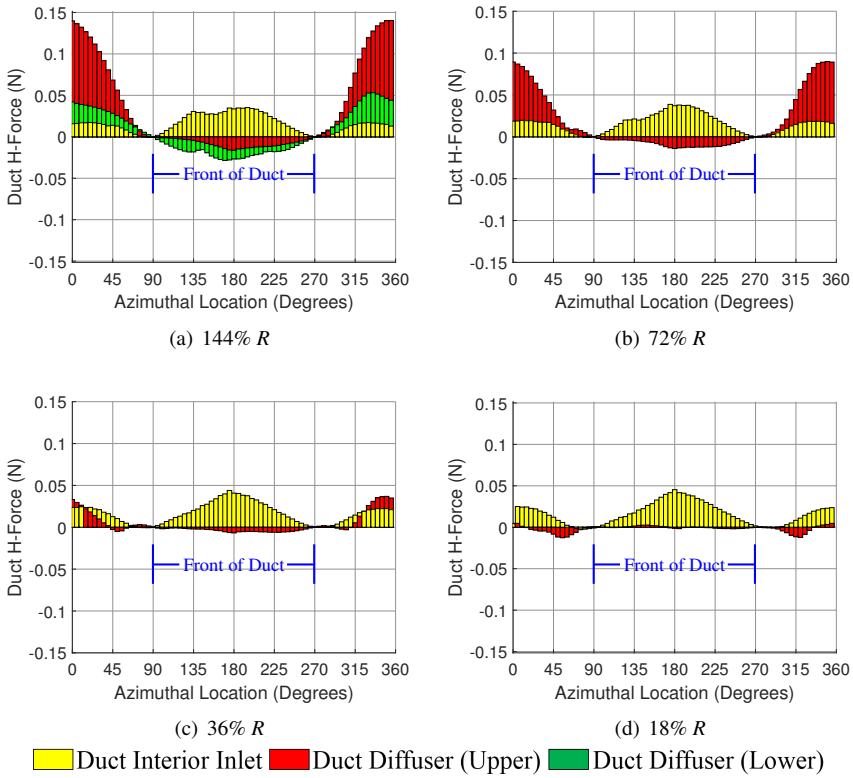

(a) 144% R (b) 72% R

(c) 36% R (d) 18% R

Duct Interior Inlet Duct Diffuser (Upper) Duct Diffuser (Lower)

Fig. 13. Azimuthal breakup of duct H-force at 10 m/s forward flight conditions averaged over one rotor revolution for various diffuser lengths

The other major contributor to duct H-force comes from the ram pressure at the rear of the duct as seen in Figure 14, which shows pressure controus on the duct at 10 m/s. The rotor induces an inflow which attempts to turn the flow 90° from the freestream to become aligned with the vertical axis of the duct. However, when the induced inflow velocity is much lower than the freestream velocity the rotor only manages to turn the air slightly downward. This flow collides with the rear of the duct near and below the rotor plane. The location of this stagnation area vertically on the duct will depend on the magnitude of the rotor induced velocity relative to the freestream velocity. This manifests as a large drag in Figure 13 (a) and is reduced dramatically by shrinking the diffuser (Figure 13 (b)-(d)). Figure 14 (b) confirms the ram pressure on the rear diffuser is eliminated. The reduction in ram pressure on the rear for shorter diffusers results from the wake more freely exiting the shorter diffuser configuration.

Figure 15 shows the generation of pitching moment around the duct at 10 m/s. The pitching moment comes predominantly from the duct thrust at the front inlet while the H-force on the duct is a secondary contributor. The azimuthal location and height relative to the rotor plane dictate the direction of the diffuser-induced pitching moment. The propulsive H-force on the front diffuser of the 144% R and 72% R induces a nose-up moment about the rotor hub. However, the positive H-force on the diffuser section at the rear of the duct, being below the rotor plane, induces a nose-down moment, though the small moment arm between the drag sources and the rotor plane reduces their net effect on generation of steady pitching moments. Furthermore, for the shorter diffuser configurations (36% R and 18% R) when the drag on the rear diffuser is reduced so too is the nose-down moment induced. Shrinking the diffuser does not affect the inlet-induced pitching moment, but does eliminate the diffuser-induced moment.

For both duct configurations the steady component of duct side force and rolling moment were small, thus an azimuthal breakup of the generation of these forces and moments is not presented.

Ducted Rotor System Performance

Figure 16 shows the thrust on the rotor and inlet (responsible for all of the duct lift) for the various diffuser lengths at 10 m/s

The rotor is the dominant source of thrust producing more than 80% of the total thrust for all diffuser lengths. The rotor thrust is insensitive to diffuser length but the duct thrust sees a reduction of 29.8% and 38.3% (compared to the longest diffuser length) when the diffuser length is decreased to 36% R and 18% R. The total thrust of the ducted rotor system decreases by 9.5% going from the 144% R to the 18% R diffuser. Rotor power is relatively unchanged regardless of diffuser length. The rotor power for each diffuser length is listed in Table 4.

The steady H-force for the different diffuser lengths at 10 m/s, shown in Figure 17, indicates that the rotor is a negligible contributor and both the rotor and inlet H-force are insensitive to diffuser length. However, the diffuser H-force, the dominant contributor, is sensitive to diffuser length. When comparing the different diffuser lengths, H-force on the diffuser can be completely eliminated by using the shorter (36% R and 18% R) diffuser lengths. Overall, the total H-force on the ducted rotor system is reduced by 67.6% by reducing the diffuser from 144% R to 18% R.

Figure 18 shows the pitching moment for the different diffuser configurations. The thrust on the front inlet (Figure 12) and the upwash region at the front of the disk (Figure 10) explain the duct inlet and rotor nose-up pitching moment. The rotor contributes over 21.2% of the total nose-up pitching moment for all diffuser lengths at 10 m/s. The rotor nose-up pitching moment for the 18% R diffuser increases by 90.8% compared to the 144% R diffuser which arises from the greater longitudinal variation in rotor thrust, specifically an increase in thrust at the front of the disk and a decrease in thrust produced by the rear (Figure 10). The upper diffuser section of the 144% R and 72% R ducts produce a nose-down pitching moment due to the ram drag at the rear of the duct, but this only partially negates the nose-up pitching moment from the inlet. Since rear diffuser drag is nearly eliminated with the shortest diffusers (36% R and 18% R), the upper diffuser no longer contributes a nose-down moment. The ducted rotor system total nose-up pitching moment of the 18% R diffuser increases by 115.3% compared to the 144% R diffuser length.

While this is a significant increase, the reduction in H-force is a substantial savings. Implementing these shorter diffuser ducted rotors in an aircraft design would benefit from the reduction in drag and the increase in pitching moment can be addressed at the aircraft level with a longitudinal configuration of rotors like the Phantom Swift (Ref. 1) or longitudinally spaced wings/control surfaces.

Finally, the steady side force from all duct configurations was observed to be negligible compared to the dominant forces and moments of the system (thrust, H-force, and pitching moment); the calculated values are at the limit of the accuracy level of this study. Similarly, while the duct does not produce a significant steady roll moment, the rotor produces a strong roll left moment but is insensitive to diffuser length. The rotor roll moments are tabulated in Table 5.

Table 4. Calculated rotor power for various diffuser lengths at 10 m/s forward flight speed

Configuration	Power (W)
18% R	38.9
36% R	40.5
72% R	39.6
144% R	39.5

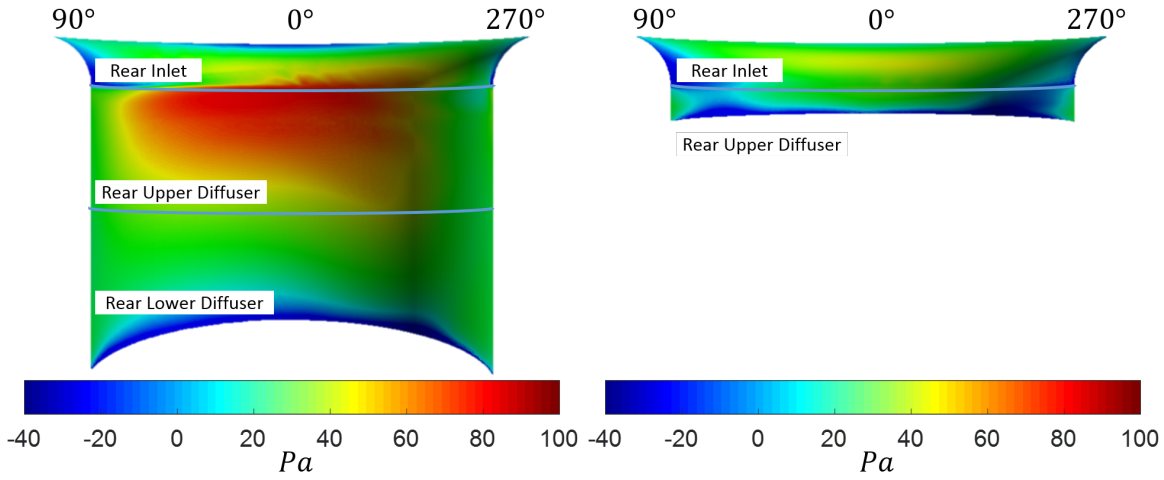

(a) 144% *R* (b) 18% *R*

Fig. 14. Pressure over rear half of duct surface (looking from the rotor hub) for 10 m/s forward flight case

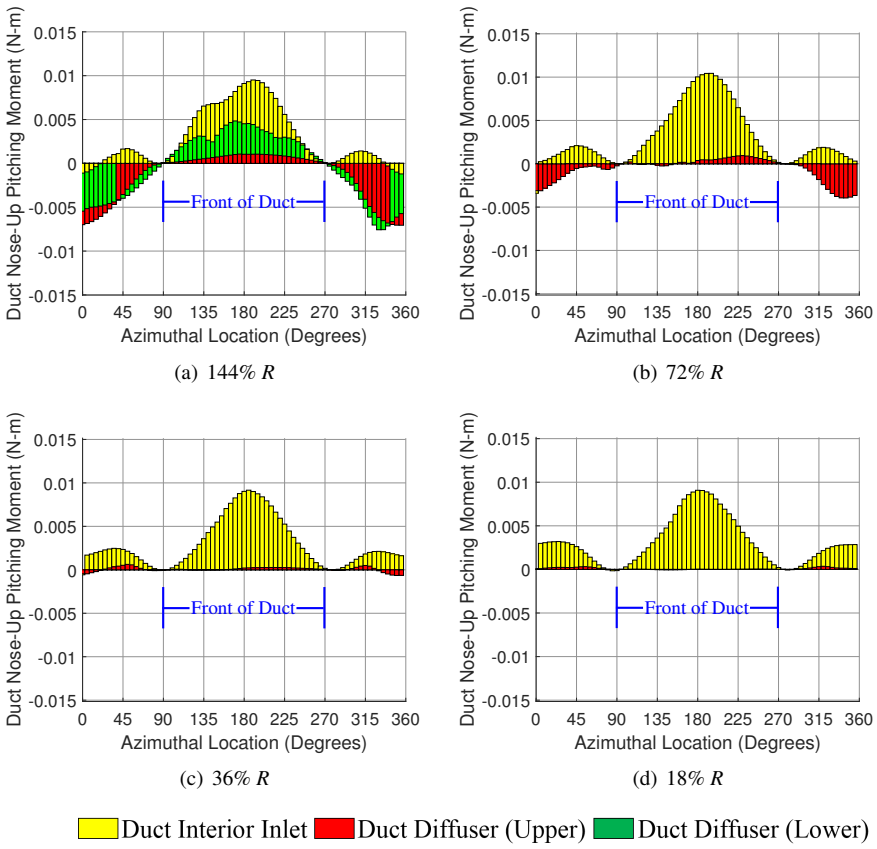

(a) 144% *R* (b) 72% *R*

(c) 36% *R* (d) 18% *R*

Fig. 15. Azimuthal breakup of duct pitching moment at 10 m/s forward flight conditions averaged over one rotor revolution for various diffuser lengths

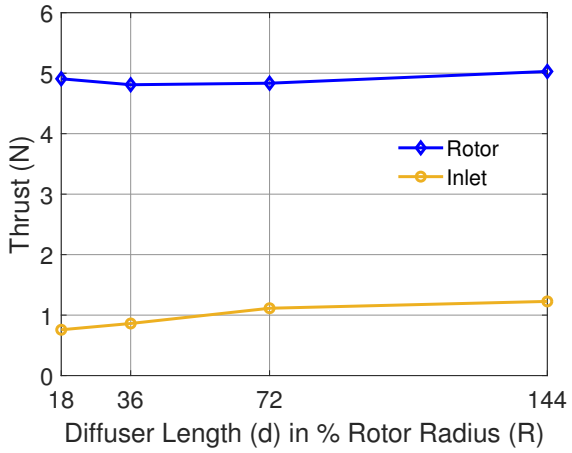

Fig. 16. Thrust of rotor and inlet compared for different diffuser lengths at 10 m/s

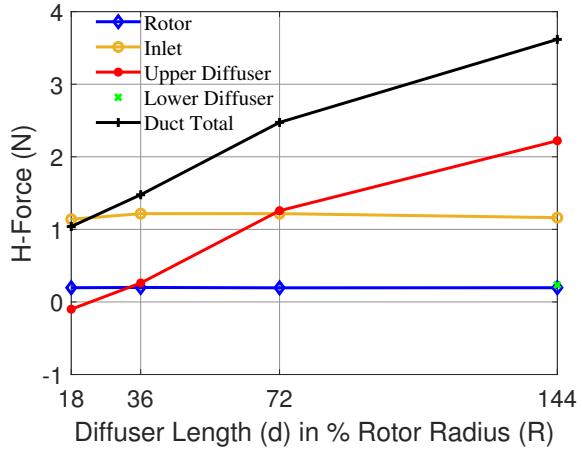

Fig. 17. H-force of rotor and duct surfaces compared for diffuser diffuser lengths at 10 m/s

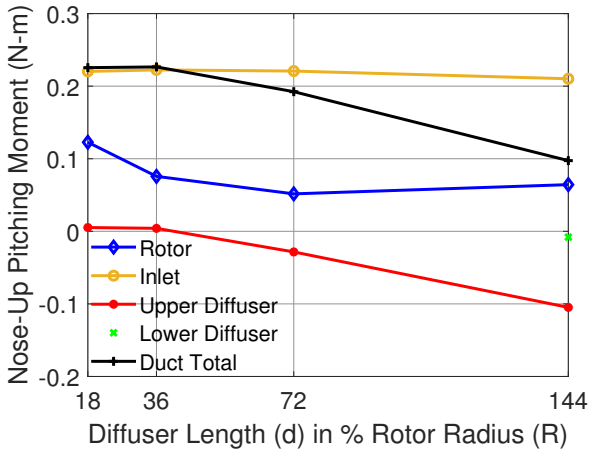

Fig. 18. Nose-up pitching moment of rotor and duct surfaces compared for diffuser diffuser lengths at 10 m/s

Table 5. Calculated rotor roll left moment for various diffuser lengths at 10 m/s forward flight speed

Diffuser Length (%R)	Roll Left Moment (N-m)
18	0.0673
36	0.0633
72	0.0618
144	0.0606

Vibratory Loads

In addition to the steady hub loads, the vibratory loads associated with the blade passage frequency were also analyzed as part of this study. Both the rotor and the duct are sources of vertical and in-plane vibrations. The rotor vertical and in-plane vibrations come from azimuthal variation in the blade root vertical shear S_z and chordwise shear S_x. Figure 19 shows the blade root vertical shear at 10 m/s forward speed for each of the diffuser lengths over a full revolution. The $S_{z_{2p}}$ of each blade contributes to the rotor hub 2/rev vertical vibratory loads in the non-rotating system while the $S_{z_{1p}}$ vibrations are canceled at the hub for a two-bladed rotor. Although the peak-to-peak variation in S_z loads is greatest for the 18% R diffuser case, the 2/rev component is 62.4% smaller than the 144% R diffuser.

Figure 20 shows the blade chordwise (drag) shear loads over one revolution. Note that the magnitude of $S_{x_{1p}}$ vibration, is the dominant source of the 2/rev rotor hub in-plane vibrations. The magnitude of the 1/rev and 2/rev for the vertical and chordwise shears can be seen in Table 6.

Table 6. Magnitude of the vibratory components of blade root shears contributing to rotor vibrations

	Diffuser Length (%R)			
	18	36	72	144
S_{z_0}	2.437	2.393	2.396	2.508
$S_{z_{1p}}$	1.341	1.012	0.918	0.922
$S_{z_{2p}}$	0.163	0.122	0.286	0.433
S_{x_0}	0.512	0.527	0.514	0.518
$S_{x_{1p}}$	0.222	0.216	0.207	0.211
$S_{x_{2p}}$	0.0376	0.0279	0.0221	0.0222

The duct is also a significant contributor to the in-plane vibrations. Due to the very small clearance between the rotor tip and duct wall, the high pressure on the lower surface and the low pressure on the upper surface near the blade tip exert local forces on the duct. Figure 21 shows the pressure on the surface of the duct immediately adjacent to the blade tip at various azimuthal locations for the 144% R and 18% R duct configurations. A component of these forces on the duct inlet act in the vertical direction resulting in a small duct contribution to vertical vibrations (Figure 22).

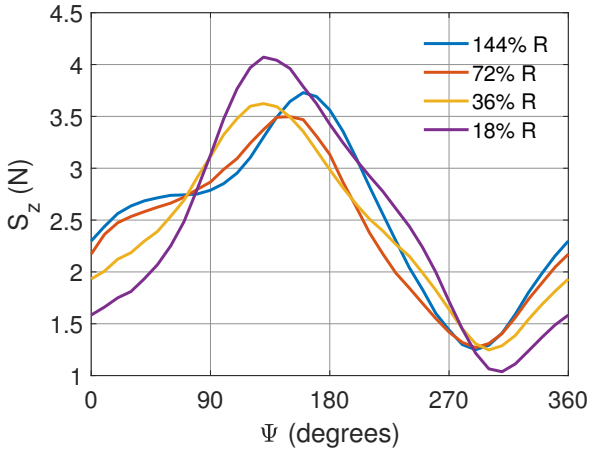

Fig. 19. Blade root vertical shear forces over one revolution at 10 m/s for various diffuser lengths

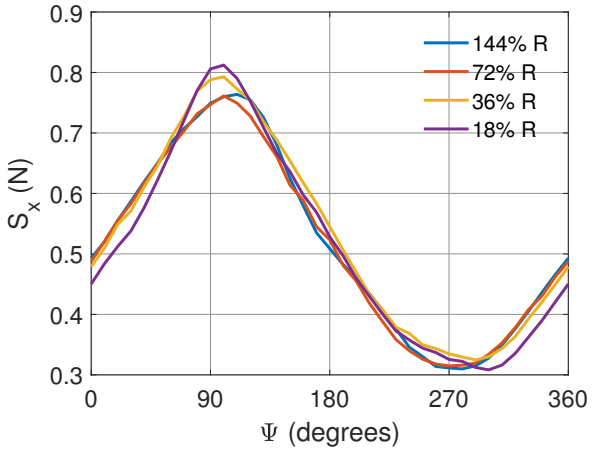

Fig. 20. Blade root chordwise shear forces over one revolution at 10 m/s for various diffuser lengths

Note in Figure 21 the suction on the duct above the blade tip inlet and the higher pressure on the duct wall below the rotor tip (upper diffuser) at any azimuthal location do not cancel, resulting in a net force that contributes to in-plane vibratory loads. Additionally, the magnitude of the in-plane H-forces generated at the front of the disk ($\Psi = 180^\circ$ on Figure 21) are much higher than those at the rear (due to the higher lift generated by the rotor blades at the front), creating further azimuthal variation in in-plane forces on the duct. The suction above the blade and high pressure below the blade also induces a net moment about the rotor plane. For the 18% *R* diffuser the magnitude of the high pressure region on the upper diffuser is small than the 144% *R* configuration, however, the suction on the inlet is of similar magnitude between the two diffuser lengths.

The vibration amplitudes were examined in forward flight at 10 m/s. The contribution of each duct surface was analyzed separately and the vibratory signals of the duct and rotor were the summed vectorially to assess the vibratory loads of the full ducted rotor system.

Figure 22 shows the magnitude of the 2/rev vertical vibrations for the different diffuser lengths. The rotor is the largest contributor to total aircraft vertical vibrations but both the rotor and duct vertical vibration magnitudes decrease with shorter diffuser lengths. Comparing the vertical vibrations shows that the 18% *R* diffuser decreases the magnitude of the 2/rev vibration by 62% compared to the 144% *R* configuration. For the 144% *R* diffuser, the rotor vertical vibration magnitude is 17.2% of the steady thrust but that magnitude is reduced to 6.6% of the steady thrust for the 18% *R* diffuser. The duct inlet is the only duct surface that significantly contributes to the vertical vibrations and it only has a significant contribution for the longer diffuser designs (72% *R* and 144% *R*).

While the steady values of side force and rolling moment were negligible, the amplitudes of the vibratory loads are of similar magnitude to the H-force and pitching moment vibrations respectively. Figure 23 shows that the H-force vibratory loads in the longitudinal direction have significant magnitude, the contributions of the rotor and duct to the side force vibrations are nearly equal in magnitude for each diffuser length though not shown in this paper. For the H-force vibratory loads, the magnitude of the vibrations decreases as the diffuser gets shorter. The rotor and diffuser vibrations are in phase while the inlet is 180° out of phase with the diffuser. The inlet being completely out of phase for in-plane vibrations occurs because of the pressures interacting with the duct associated with blade passage. The suction on the inlet results in a force towards the center of the duct while the pressure on the diffuser exerts an outward force. The The H-force 2/rev vibration magnitude of the 18% *R* diffuser is 69% lower than the 144% *R* configuration due to the reduction in diffuser area. The magnitude of the full ducted rotor system H-force vibrations is approximately 10% of the steady H-force at all diffuser lengths, the reduction in H-force vibrations with shorter diffuser lengths decreases at the same rate as the steady H-force of the system.

Similar to the in-plane vibrations, the vibratory pitching and rolling moment are comparable in magnitude when analyzed at the 10 m/s and thus only the pitching moment vibrations are presented. Figure 24 show the rotor is the largest contributor to the vibratory moments and now the rotor, inlet, and diffuser induce vibrations in phase with each other. The forces acting in opposite directions on the inlet and diffuser now induce pitching and rolling moments about the rotor plane that are in the same direction. Unlike the H-force vibrations, the magnitude of the pitchining moment 2/rev vibrations for the 18% diffuser increases by 18% compared to the 144% *R* diffuser that result from an increase in rotor pitching moment vibrations. The magnitude of the full ducted rotor system pitching moment vibrations are 73.8% of the steady total pitching moment at 10 m/s for the 144% *R* diffuser. While the magnitude of the pitching moment vibrations is highest for the 18% *R* diffuser, the vibratory load magnitude is 40.6% of the steady nose-up pitching moment in forward flight.

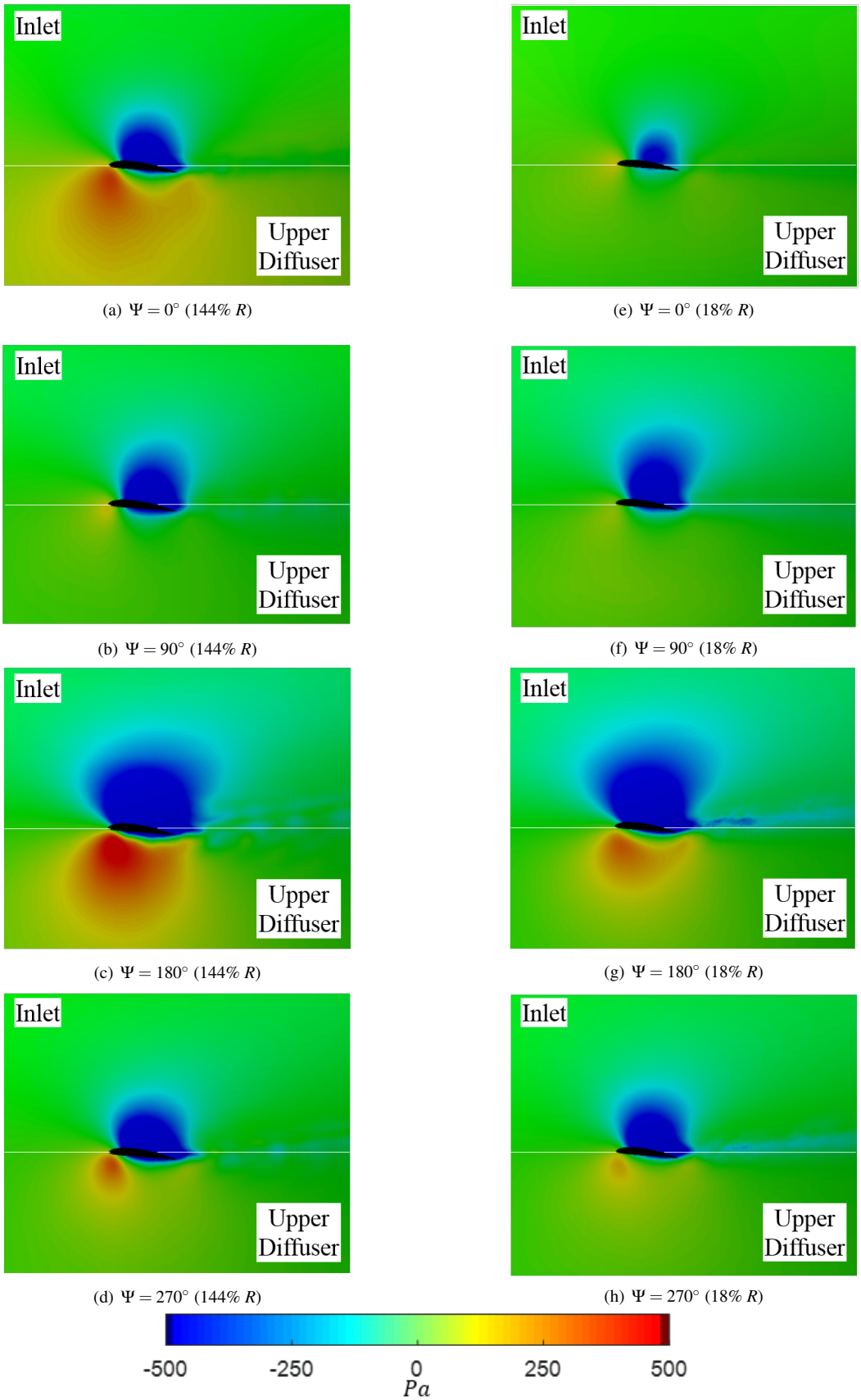

(a) $\Psi = 0°$ (144% R)

(e) $\Psi = 0°$ (18% R)

(b) $\Psi = 90°$ (144% R)

(f) $\Psi = 90°$ (18% R)

(c) $\Psi = 180°$ (144% R)

(g) $\Psi = 180°$ (18% R)

(d) $\Psi = 270°$ (144% R)

(h) $\Psi = 270°$ (18% R)

Fig. 21. Pressure contours on duct inlet and upper diffuser adjacent to rotor tip at various azimuth positions corresponding to the 144% R (a,b,c,d) and 18% R (e,f,g,h) configurations

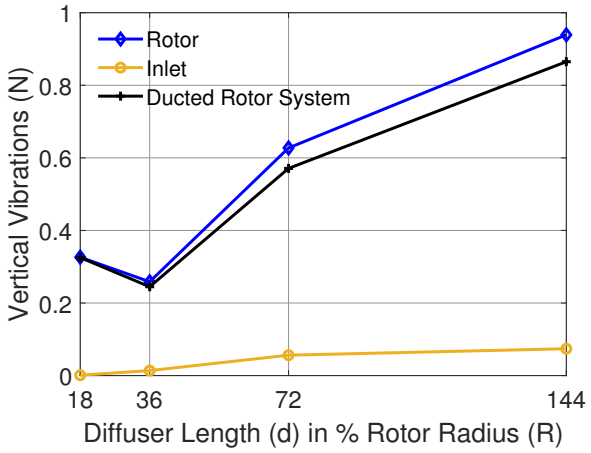

Fig. 22. Ducted rotor 2/rev vertical vibration magnitudes at 10 m/s forward flight speed

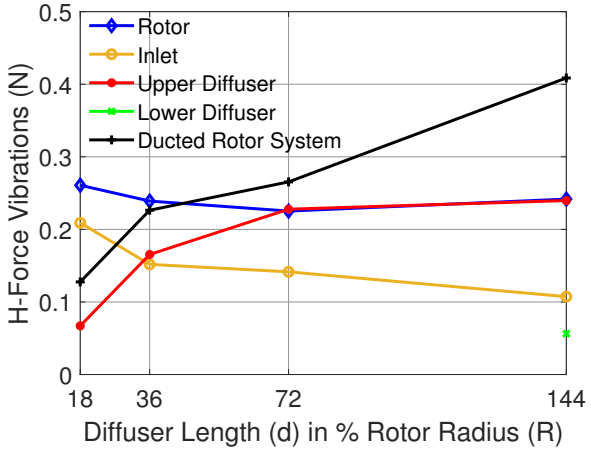

Fig. 23. Ducted rotor 2/rev H-force vibration magnitudes at 10 m/s forward flight speed

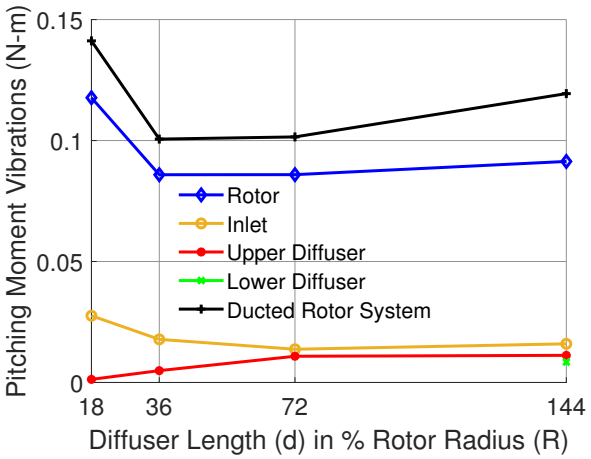

Fig. 24. Ducted rotor 2/rev pitching moment vibration magnitudes at 10 m/s forward flight speed

CONCLUSIONS

Using a three dimensional RANS CFD model, ducted rotors with various diffuser lengths were simulated with a sliding mesh to analyze its behavior in hover and forward flight conditions given zero nose down attitude. This study examined the rotor and interior sections of the duct and determined the influence of each component on the performance, and provides a comparison between the configurations. A detailed examination of the flow physics was used to understand the differences in the ducted rotor behavior due to different diffuser lengths. The dominant steady forces and moments were analyzed as well as the vibratory loads on the ducted rotor system. The complex flow phenomena and rotor-duct interactions are explained as they pertain to the performance.

In hover the shorter diffuser configurations (18% and 36% R) were observed to produce $\sim$ 3% less total thrust than the longer diffuser configurations (72% and 144% R) but both the shorter and longer diffuser configurations produced more total thrust than the open rotor by $\sim$ 26% and $\sim$ 30% respectively. Decreasing the length of the diffuser from 144% R to 18% R was shown to only increase the rotor power by $\sim$ 1.5%. The ducted rotors achieved higher power loading by $\sim$ 5% for the shorter diffusers and by $\sim$ 10% for the longer diffuser configurations, relative to an open rotor at the same RPM.

For 10 m/s forward flight conditions the ducted rotors produce the majority of their thrust at the front of the disk due to upwash increasing the effective angle of attack of the blades. As diffuser length was decreased, the thrust produced by the rear of the rotor disk also decreased but slightly more thrust was produced at the front of the disk resulting in total rotor thrust being insensitive to diffuser length but the rotor nose-up pitching moment increasing by 90.8% when the diffuser length is reduced from 144% to 18% R. Unlike the maximum thrust which is seen at the front of the disk, the maximum rotor drag is observed on the advancing side. At the front of the disk although the lift is the highest the upwash reduces the induced drag, thereby limiting the total drag. The maximum drag on the advancing side is observed in the mid-span region rather than the outboard sections due to the high twist and taper ratio of the blade. Lastly, the rotor power is insensitive to diffuser length and the rotor is a small contributor to total H-force providing 15% at most for the 18% R configuration and only 5% for the 144% R diffuser.

With regards to the duct, all configurations produce the majority of the thrust on the front inlet, though the 18% R diffuser produces 38% less thrust than the 144% R configuration. The duct H-force comes predominantly from a combination of a component of the suction on the front inlet and ram pressure on the rear diffuser. Decreasing the length of the diffuser to 18% R was shown to reduce the duct H-force by 71% compared to the 144% R diffuser due to elimination of ram pressure on the rear diffuser. The duct total nose-up pitching moment is increased by 132% when decreasing the diffuser length from 144% to 18% R due to the reduction in H-force on the rear diffuser that provides a compensatory nose-down moment for the longer diffuser configurations.

The vertical vibrations of all diffuser configurations come primarily from the rotor. The magnitude of the 18% *R* 2/rev rotor vertical vibrations are reduced by 62% compared to the 144% *R* configuration. The local pressure on the duct walls due to blade passage produces in-plane vibrations at the blade passage frequency. The magnitude of these vibrations, being tied to the instantaneous thrust produced by the nearby blade tip, are reduced for the shorter diffuser lengths, where the high pressure region below the blade has less diffuser area to act on. The magnitude H-force vibrations for the 18% *R* diffuser are 69% lower than the 144% *R* configuration. The 18% *R* configuration has 18% larger magnitude of pitching moment vibrations than the 144% *R* diffuser.

ACKNOWLEDGMENTS

The authors would like to thank Rensselaer Polytechnic Institute and the Center for Computational Innovations. The findings from this study are only possible thanks to the availability of their computing resources and dedicated staff that maintain the network and hardware.

REFERENCES

[1]Ziegenbein, P., "PhantomSwift Quad-Ducted Rotor Aircraft Configuration Development," in *American Helicopter Society 72nd Annual Forum, West Palm Beach, FL*, May 2016.

[2]Tatro, J., Yoeli, R., and Samples, D., "X-Hawk: Transformational Mobility for the Urban Warfighter," in *American Helicopter Society 62nd Annual Forum, Phoenix, AZ, May*, May 2006.

[3]Hirschberg, M., "On Wind Tunnel Tests and Computations Concerning the Problem of Shrouded Propellers," *Vertiflite*, pp. 10–11, Aug. 2016.

[4]Kruger, W., "On wind tunnel tests and computations concerning the problem of shrouded propellers - tn 1202," tech. rep., NACA, 1949.

[5]Leishman, J. G., *Principles of Helicopter Aerodynamics*. Cambridge University Press, 2nd ed., 2006.

[6]Platt Jr., R., P., "Static Tests of a Shrouded and an Unshrouded Propeller," techreport L7H25, National Advisory Committee for Aeronautics, Feb. 1948.

[7]Taylor, R., T., "Experimental Investigation of the Effects of Some Shroud Design Variables on the Static Thrust Characteristics of Small-Scale Shrouded Propeller Submerged in a Wing," techreport 4126, National Advisory Committee for Aeronautics, Jan. 1958.

[8]Pereira, J. and Chopra, I., "Surface Pressure Measurements on an MAV-Scale Shrouded Rotor in Hover," in *American Helicopter Society 62nd Annual Forum, Phoenix, AZ*, May 2006.

[9]Pereira, J. and Chopra, I., "Performance and Surface Pressure Measurements on a MAV-Scale Shrouded Rotor in Translational Flight," in *American Helicopter Society 63rd Annual Forum, Virginia Beach, VA*, May 2007.

[10]Hook, R., Myers, L., and McLaughlin, D., "Investigation on Flow Physics of Edgewise Ducted rotor Air Vehicles," in *American Helicopter Society 67th Annual Forum, Virginia Beach, VA*, May 2011.

[11]Hook, R., Myers, L., and McLaughlin, D., "A Study of Leading Edge Shapes for the Front Duct of a Dual Ducted Rotor Vehicle," in *American Helicopter Society 67th Annual Forum, Virginia Beach, VA*, May 2011.

[12]Martin, P., and Tung, C., "Performance and Flowfield Measurements on a 10-inch Ducted Rotor VTOL UAV," in *American Helicopter Society 60th Annual Forum, Baltimore, MD, June*, June 2004.

[13]Martin, P., and Boxwell, D., A., "Design, Analysis and Experiments on a 10-Inch Ducted Rotor VTOL UAV," in *American Helicopter Society International Specialists Meeting on Unmanned Rotorcraft: Design, Control and Testing, Chandler, AZ, Jan*, Jan. 2005.

[14]Akturk, A., and Camci, C., "Influence of Tip Clearance and Inlet Flow Distortion on Ducted rotor Performance in VTOL UAVs," in *American Helicopter Society 66th Annual Forum, Phoenix, AZ*, May 2010.

[15]Akturk, A., and Camci, C., "Experimental and Computational Assessment of a Ducted-Fan Rotor Flow Model," *Journal of Aircraft*, vol. 49, pp. 885–897, May-June 2012.

[16]Akturk, A., and Camci, C., "Lip separation and Inlet Flow Distortion Control in Ducted Fans Used in VTOL Systems," in *ASME Turbo Expo, Dusseldorf, Germany*, June 2014.

[17]Singh, R., and Dinavahi, S., "Shape Optimization of a Ducted Rotor System for Aerodynamic Performance," in *49th AIAA Aerospace Sciences Meeting, Orlando, FL*, January 2011.

[18]Jimenez, B., and Singh, R., "Effect of Duct-Rotor Aerodynamic Interactions on Blade Design for Hover and Axial Flight," in *53rd AIAA Aerospace Sciences Meeting, AIAA SciTech, Kissimmee, FL*, January 2015.

[19]Misiorowski, M., Gandhi, F., and Oberai, A., "Computational Analysis and Flow Visualization of Ducted Rotors in Edgewise Flight," in *American Helicopter Society 73rd Annual Forum, Fort Worth, TX*, May 2017.

[20]Misiorowski, M., Gandhi, F., and Oberai, A., "Computational Analysis of Isolated and Embedded Ducted Rotors in Edgewise Flight," in *American Institute of Aeronautics and Astronautics SciTech Forum, Orlando, Florida*, Jan. 2018.

[21]Wang, J., "Technical Considerations in the Designing of the AgustaWestland Project Zero - World First Full-Size Electric VTOL Aircraft," (San Francisco), American Helicopter Society, Jan. 2014.

[22]Advanced Precision Composites - Propellers, "Performance Data - 12x5.5 MR," tech. rep., APC, 2014.

[23]Corson, D., Rajeev, J., and Farzin, S., "Industrial Application of RANS Modeling: Capabilities and Needs," *International Journal of Computational Fluid Dynamics*, vol. 23, no. 4, pp. 337–347, 2009.

[24]Shur, M., L., Spalart, P., Strelets, M., and Travin, A., "Detached Eddy Simulation of an Airfoil at High Angle of Attack," in *Engineering Turbulence Modelling and Experimetns* (Rodi, W., and Laurence, D., ed.), no. 4, pp. 669–678, Elsevier Science Ltd., Dec. 1999.

[25]Simmetrix, "MeshSim Automatic Mesh Generation." May 1997.

[26]Jansen, K., E., Whiting, C., H., and Hulbert, G., M.,, "A generalized-α method for integrating the filtered navier-stokes equations with a stabilized finite element method," *Computer Methods in Applied Mechanics and Engineering*, vol. 190, no. 3, pp. 305–319, 2000.

[27]Brooks, A., N., and Hughes, T., J., "Streamline Upwind/Petrov-Galerkin Formulations for Convection Dominated Flows with Particular Emphasis on the Incompressible Navier-Stokes Equations," *Computer Methods in Applied Mechanics and Engineering*, vol. 32, no. 1-3, pp. 199–259, 1982.